Temperature-Dependent Ion Migration Underlies Sequence-Specific Collapse of Unstructured RNA

Heyang Zhang,[†] Hiranmay Maity,[†,‡] and Hung T. Nguyen[*,†]

†*Department of Chemistry, State University of New York at Buffalo, Buffalo, New York 14260-3000, United States*

‡*Department of General Sciences, Birla Institute of Technology and Science, Pilani, Dubai Campus, Dubai International Academic City, Dubai 345055, UAE*

E-mail: nguyenh@buffalo.edu

Abstract

Ions and temperature jointly regulate RNA structure, dynamics and phase behavior, yet their coupled effects remain poorly understood at the molecular level. Single-stranded RNA (ssRNA), a ubiquitous and functionally versatile class of RNA, presents a particularly challenging target due to its intrinsic flexibility and pronounced sensitivity to ionic and thermal perturbations. Here, we extend our previously validated coarse-grained RNA model by introducing temperature-dependent divalent ion-phosphate potentials along with revised stacking interactions to elucidate how electrostatics, stacking, and hydration collectively determine ssRNA behavior. Our simulations quantitatively reproduce experimental SAXS profiles across a broad range of ionic conditions and reveal a non-monotonic temperature dependence of RNA compaction: ssRNAs expand upon heating, reach a sequence-specific

maximum size, and then collapse as enhanced counterion condensation dominates. Rising temperature strengthens ion-RNA interactions, leading to a reorganization from diffusive to inner-sphere coordination, directly linking RNA collapse to ion dehydration. Our results establish that the ion atmosphere is a dynamic, sequence-encoded extension of RNA structure. This framework provides molecular insight into how temperature and ions govern RNA conformational transitions, offering a microscopic basis for RNA thermoadaptation, cold-induced misfolding, and RNA phase transitions.

Graphical Abstract

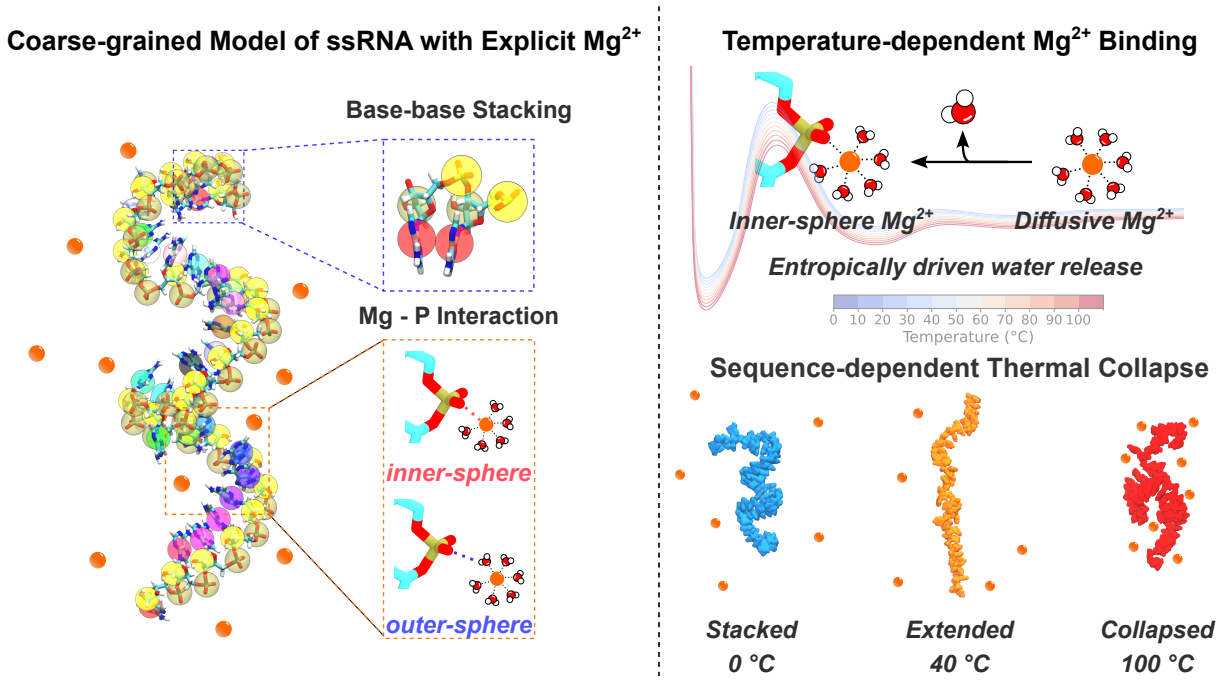

Introduction

RNA plays a central role in virtually all biological processes, with its function intricately linked to its structure.[1–7] The structural landscape of RNA is highly dynamic and shaped by a wide range of intrinsic and extrinsic factors,[8] including the primary sequence,[9] physiological conditions,[7] ion concentrations,[10–14] molecular interactions with other biomolecules,[15,16] as well as covalent RNA modifications.[17–20] Among its diverse structural motifs, single-stranded RNA (ssRNA) is particularly versatile. Beyond serving as linkers between structured regions, ssRNA contributes to higher-order RNA architecture and functions as regulatory elements throughout the mRNA lifecycle.[21–26] A wide array of cellular proteins, including those that are highly expressed, exhibit selective affinity for ssRNA, mediating essential steps in gene expression at both the transcriptional and post-transcriptional levels.[27–31]

The interactions between ssRNAs and regulatory proteins are expected to be dependent on sequence-specific structures. However, the molecular mechanisms underlying many processes involving ssRNAs remain poorly understood, primarily due to the limited understanding of their structural features. This challenge has persisted since the pioneering studies of the late 1950s.[32] Early experimental techniques provided the fundamental insights for both intrinsic and extrinsic factors influencing the single-stranded helices of poly(rA), poly(rU), and poly(rC).[33–44] In contrast, poly(rG) readily self-associates into higher-order structures, most notably the G-quadruplex.[45] These studies identified base stacking as a dominant energetic determinant of helix formation, with temperature and ion concentration significantly impacting the helix formation kinetics.[46] Subsequent experimental advances have highlighted the substantial effects of Mg^{2+} on the structures of ssRNA.[47–51] More recently, with growing interest in understanding biomolecular condensates, ssRNA has been shown to interact with arginine/glycine-rich intrinsically disorder regions, affecting the viscoelastic and dynamic properties of these condensates.[52–56] Short poly(rA) sequences form Mg^{2+}-dependent condensates, yet the structural organization of ssRNA within these assemblies remains largely unknown.[57]

In principle, atomistic MD simulations can be used to probe ssRNA conformational ensembles, but their accuracy remains limited by imperfect force fields, which often lead to unrealistic collapse and inadequate treatment of ion effects.[58–65] Recent calibration in ion-phosphate interactions has enabled more accurate simulations of ion effects on RNA structure and dynamics.[52,66–68] However, due to the restrictions in timescale and system size accessible in all-atom simulations,[63] their application to ion-induced RNA folding and condensate formation is limited. Coarse-grained (CG) models provide a more computationally efficient alternative, although most have focused on well-folded sequences.[69–73] Several recent CG approaches tend to overestimate ssRNA size, likely due to oversimplified base-stacking representations and *ad hoc* treatments of ion-RNA interactions.[74–76] Nonetheless, the qualitative insights provided by these models remain important for shaping our understanding of RNA behavior. We recently extended our Single-Interaction-Site (SIS) model[77] by incorporating explicit Mg^{2+}-RNA interactions, revealing the more extension of ssRNA ion atmosphere.[78] However, the SIS model, in its current form, cannot realistically account for base-stacking, thus failing to model the sequence effects on ssRNA structural ensemble.

To overcome these limitations, we resorted to the Three-Interaction-Sites (TIS) model of RNA, where each nucleotide is represented by three CG beads corresponding to the ribose, phosphate, and nucleobase groups (Fig. 1).[70] In this work, we further develop temperature-dependent potentials of mean force (PMFs) for divalent ion-phosphate interactions, extending our previously reported model[79] to incorporate thermal effects via liquid-state integral equation theory.[80–83] The resulting PMFs naturally capture both inner- and outer-sphere coordination of Mg^{2+} with RNA, while interactions involving monovalent ions are treated implicitly through a mean-field Debye–Hückel (DH) term. Compared to our earlier model,[79] the present implementation introduces revised functional forms and an optimized parameter set (see Methods section). These refinements improve numerical stability and yield a more accurate balance among base stacking, backbone flexibility, and electrostatic interactions.

Using unbiased CG simulations, we find excellent agreement between the calculated

ssRNA conformational ensembles and experimental small-angle X-ray scattering (SAXS) data,[50] capturing transient helical structures populated by rA_{30}. More importantly, we revealed a pronounced temperature dependence of ssRNA conformations and ion distributions. As temperature increases, RNA undergoes a non-monotonic transition, first expanding and subsequently collapsing, due to the interplay between base unstacking and temperature-enhanced ion-mediated attractions. Strikingly, we observed a reorganization of the ion atmosphere at elevated temperatures in which diffuse ions condense inward to form direct contacts with the phosphate backbone, leading to the partial collapse of the extended ion cloud. Together, these findings establish a robust computational framework for investigating the structural and electrostatic features of RNA under varying ionic and thermal conditions.

Methods

Three-interaction-site (TIS) RNA model with explicit Mg^{2+}. The TIS model represents each nucleotide with three spherical beads (interaction sites), corresponding to the phosphate, ribose and nucleobase.[84] The beads are positioned at the center-of-mass (COM) of the chemical groups (Fig. 1).

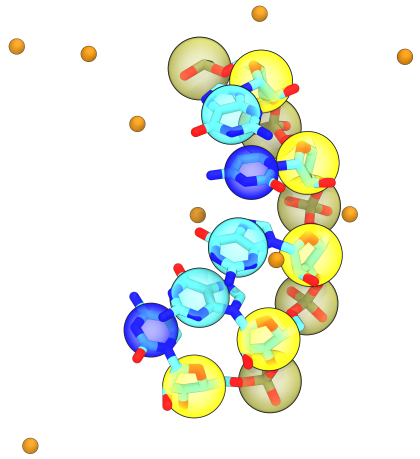

Figure 1: Three-interaction-site (TIS) representation of RNA. Beads represent the ribose, phosphate, and base, with explicit Mg^{2+} ions.

The details of the model are presented elsewhere.[79,84] Briefly, the energy function describing the interactions between RNA beads is expressed as a sum of contributions from the bond length (U_{BL}), bond angle (U_{BA}), single-stranded stacking (U_{ST}), hydrogen bonding (U_{HB}), excluded volume (U_{EV}), and electrostatic (U_{EL}) interactions (Eq. 1):

$$U_{TIS} = U_{BL} + U_{BA} + U_{ST} + U_{HB} + U_{EV} + U_{EL}. \tag{1}$$

We use the harmonic approximation for U_{BL} and U_{BA}, where the equilibrium values (k_b, k_θ, r_0, and θ_0) are listed in Tables S1 and S2. Excluded volume interactions are modeled using the Weeks–Chandler–Andersen (WCA) potential[85] (Eq. 2):

$$U_{EV} = \begin{cases} \varepsilon_0 \left[\left(\frac{D_0}{r}\right)^{12} - 2\left(\frac{D_0}{r}\right)^{6} + 1 \right], & r \leq D_0 \\ 0, & r > D_0 \end{cases}, \tag{2}$$

where $\varepsilon_0 = 1$ kcal/mol and $D_0 = R_i + R_j$. R_i for ions and RNA beads are listed in Table S3. The WCA term vanishes if the interacting sites are separated by a distance greater than D_0. For interactions between two bases, we set $D_0 = 3.2$ Å to favor stacking.

Stacking potential. Stacking interactions U_{ST} are applied to any two consecutive nucleotides along the chain (Eq. 3):

$$U_{ST} = \frac{U_{ST}^0}{1 + k_r(r - r_0)^2 + k_\phi(|\phi_1 - \phi_{1,0} - \pi| - \pi)^2 + k_\phi(|\phi_2 - \phi_{2,0} + \pi| - \pi)^2}, \tag{3}$$

where r is the distance between B_i and B_{i+1}, $\phi_1(P_i, S_i, P_{i+1}, S_{i+1})$ and $\phi_2(P_{i+2}, S_{i+1}, P_{i+1}, S_i)$ are dihedral angles around the sugar-phosphate bonds (Fig. 2A). The absolute values ensure the dihedral angles are continuously wrapped around $-\pi$ and π (Fig. S1B) and $(|\phi_2| - \phi_{2,0})^2$ (Fig. S1E), such that positive and negative dihedrals are treated equivalently. To avoid generating two minima, we shift the functional form so that a single minimum occurs between $-\pi$ and π, while preserving the shape of the potential elsewhere (Fig. 2B and Fig. S1C, F).

The structural reference parameters r_0, $\phi_{1,0}$, and $\phi_{2,0}$ were obtained by coarse-graining an A-form RNA helix,[86] where the dihedral angles were averaged to yield $\phi_{1,0} = -2.587$ rad and $\phi_{2,0} = 3.071$ rad. Previous simulations suggested $k_r = 1.4$ and $k_\phi = 4$ rad^{-2} to reproduce the fluctuations of $(r - r_0)^2$, $(\phi_1 - \phi_{1,0})^2$ and $(\phi_2 - \phi_{2,0})^2$ observed in NMR structure.[84]

To recalibrate the model, we simulate base stacking of all 16 RNA dinucleotides. We use the stacking potential U_{ST} described in Eq. 3 with $U^0_{ST} = -h + k_B(T - T_m)s$ where T is the temperature (in Kelvin), and h and s are adjustable parameters representing enthalpic and entropic contributions, respectively. The stacking free energy for each dimer is then calculated using $G = -k_B T \ln \frac{p}{1-p}$ where p is the fraction of stacked configurations satisfying $U_{ST} < -k_B T$ (Figs. S20 - S35). The optimized h and s parameters used in simulations are listed in Table S4. The simulated thermodynamics parameters have excellent agreement with experimentally derived values (Fig. 2C).[84,87]

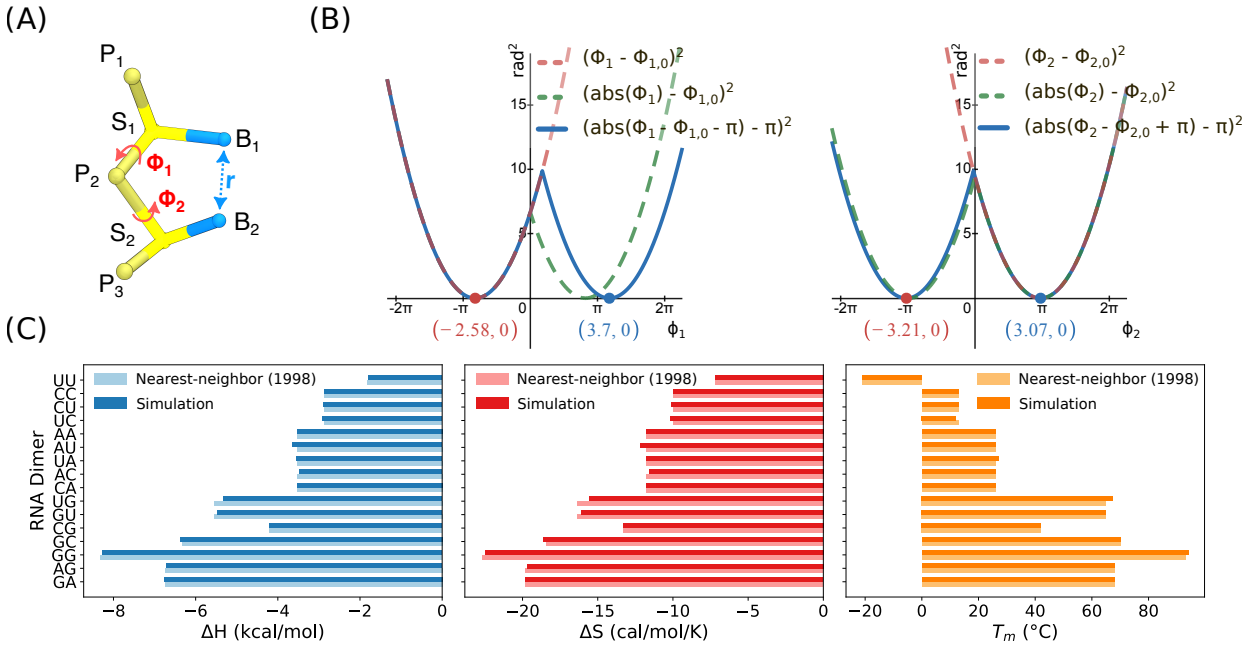

Figure 2: Calibration of RNA stacking parameters. **(A)** Illustration of the structural parameters defined in Eq. 3. **(B)** *Left:* Comparison of numerical evaluations of $(\phi_1 - \phi_{1,0})^2$ with $\phi_{1,0} = -2.587$ rad, which does not wrap continuously across 0 rad (red dashed line), leading to numerical instabilities during simulation. Replacing this term with $(|\phi_1| - \phi_{1,0})^2$ restores periodicity and resolves the instability. Further shifting the function to $(\phi_1 - \phi_{1,0} - \pi| - \pi)^2$ enforces a single minimum within $[-\pi, \pi]$ while preserving the overall functional shape. *Right:* Same analysis as the left panel, but for ϕ_2 with $\phi_{2,0} = 3.071$ rad. **(C)** Calculated thermodynamic parameters reproduce values derived from the nearest-neighbor model.[87]

Temperature-Dependent Ion-Phosphate Interaction. Following our previous procedure,[79] we resort to the well-known Reference Interaction Site Model (RISM) theory to calculate the potential of mean force (PMF) between Mg^{2+} and phosphate. We use 1D-RISM[80,81,83] to calculate the radial distribution function $g_{Mg-P}(r)$, and then convert it to PMF: $W(r) = -k_B T \ln g_{Mg-P}(r)$. The theory starts with the Ornstein–Zernike (OZ) equation (Eq. 4):

$$h(r_{12}) = c(r_{12}) + \rho \int dr_3 c(r_{13}) h(r_{32}), \tag{4}$$

where r_{ij} is the distance between particles i and j, c is the direct correlation function, and h (the total correlation function) is related to g as $h(r_{ij}) = g(r_{ij}) - 1$. To solve the OZ equation, another equation (known as the closure relation) connects h and c (Eq. 5):

$$g(r_{12}) = \exp[-\beta u(r_{12}) + h(r_{12}) - c(r_{12}) + b(r_{12})], \tag{5}$$

where u_{ij} is the pairwise potential energy function and b_{ij} is an unknown "bridge function". In our work, we choose to use the partial series expansion of order-n (PSE-n) closure[88] to improve the results for highly charged systems (compared to Kovalenko–Hirata closure[89]), while circumventing the convergence issues associated with the hypernetted-chain closure[83,90,91] (Eq. 6):

$$g = \begin{cases} \exp(-\beta u + h - c) & \text{if } g \leq 1 \\ \sum_{k=0}^{n} \frac{(-\beta u + h - c)^k}{k!} & \text{if } g > 1 \end{cases}. \tag{6}$$

To ensure the effective potential has the correct long-ranged behavior in different conditions (ion, temperature, etc), we smoothly merge the short-ranged PMF $W(r)$ with the mean-field DH potential $U_{DH}(r)$ as described in previous work (Eq. 7):[79]

$$V_{Mg-P}(r) = W(r) + [U_{DH}(r) - W(r)] \exp\left(-\frac{a^2}{r^2}\right). \tag{7}$$

The parameter a is set to 5.0 Å to preserve the direct-contact binding energy of Mg^{2+}.

The resulting effective potential $V_{Mg-P}(r)$ asymptotically reaches the DH approximation at large distances, while displaying water-mediated short-ranged interactions according to RISM theory (Fig. 3).

Electrostatic interactions between other charged sites (phosphate–phosphate, and Mg^{2+}–Mg^{2+} repulsions) are treated using DH theory, which approximates the screening behavior of implicit monovalent salt buffer (Eq. 8):

$$U_{DH}(r) = \frac{l_B}{2} k_B T \sum_{i,j} \frac{Q_i Q_j \exp(-\frac{r_{ij}}{\lambda})}{r_{ij}}, \tag{8}$$

where $\lambda = (8\pi l_B \rho_1)^{-1/2}$ is the DH screening length determined by the number densities of monovalent ions, ρ_1. The Bjerrum length $l_B = \frac{e^2}{4\pi\epsilon_0\epsilon_r(T)k_B T}$ sets the strength of the interactions, where e is the elementary charge, ϵ_0 is the vacuum permittivity, and $\epsilon_r(T) = 87.74 - 0.4008T + 9.398 \times 10^{-4}T^2 - 1.410 \times 10^{-6}T^3$ is the temperature-dependent dielectric constant of water (where T is in °C).[92] The effective charge of phosphate, $Q_P(T, C_1, C_2)$, depends on concentrations of both the monovalent (C_1) and divalent ions (C_2) using counterion condensation theory[93–95] as described in our previous work.[79] This approach adjusts the bare charge of phosphate according to ion concentrations and temperature, providing effective charges that reflect ion-mediated screening and condensation in a physically consistent manner.

Langevin dynamics simulations. All simulations are performed using OpenMM 8.0.0[96] on NVIDIA A100 Graphics Processing Unit (GPU). We use LangevinMiddleIntegrator in OpenMM to integrate the equations of motion in NVT ensemble with a timestep of 2 fs. Mg^{2+} ions were initially placed at random positions within a cubic box containing the ssRNA of interest. The box size ranges from 420 Å to 720 Å, depending on the bulk Mg^{2+} concentrations, and is chosen such that at least 200 Mg^{2+} ions are present. We apply periodic boundary conditions in all three dimensions to minimize finite-size effects. We use low-friction Langevin dynamics to enhance conformational sampling, with a friction coeffi-

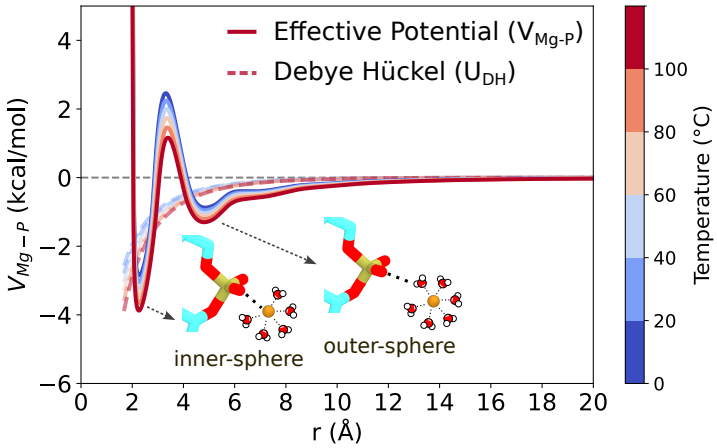

Figure 3: Temperature-dependent effective potential between Mg^{2+} and phosphate. At short distances, the potential captures both inner-sphere and outer-sphere coordination. At longer distances, it transitions smoothly to the Debye-Hückel form, reflecting electrostatic screening, and plateaus at large separations.

cient of 0.01 ps^{-1}. Snapshots are saved every 10,000 integration steps, and all trajectories are examined for equilibration and convergence before analyses.

Analyses. *Calculations of Mg^{2+} preferential interaction coefficient.* First, all frames are aligned to the ssRNA COM. The local concentration of Mg^{2+} is subsequently computed as (Eq. 9):

$$C_{Mg}(r) = \frac{N_{Mg}(r)}{\Delta V_r C_{Mg}}, \tag{9}$$

where $N_{Mg}(r)$ is the number of Mg^{2+} ions within the spherical shell of volume ΔV_r between r and $r + \Delta r$, and C_{Mg} is the initial Mg^{2+} concentration ($C_{Mg} = \frac{N}{V_S}$, where N is the total number of Mg^{2+} and V_S is the volume of the simulation box). Because ssRNA is highly negatively charged, Mg^{2+} are attracted to phosphate groups, thus the effective bulk concentration, C_{Mg}^{eff}, is lower than the initial value. We determine C_{Mg}^{eff} as the plateau value in the concentration profile $C_{Mg}(r)$ at large separation (Figs. S36, S37, and S38).

The preferential interaction coefficient (Γ_{Mg}) reports the excess number of ions associated with RNA relative to bulk solution.[97,98] We calculate Γ_{Mg} using the Kirkwood–Buff integral (Eq. 10):

$$\Gamma_{Mg} = C_{Mg}^{eff} 4\pi \int_{r=0}^{r_{cs}} [g(r) - 1] r^2 dr, \tag{10}$$

where $r_{cs} = \frac{L}{2}$ is half the simulation box length, and r is the distance from Mg^{2+} to the RNA COM.

Partitioning of inner-sphere, outer-sphere, and diffusive ions. A Mg^{2+} ion is classified as inner-sphere if the Mg-phosphate distance falls within the first peak of $g_{Mg-P}(r)$ ($r < 3.2$ Å). Mg^{2+} within the second peak (3.2 Å $< g_{Mg-P}(r) < 6.1$ Å) is assigned to the outer-sphere population. The number of diffuse ions is then computed as $N_{dif} = \Gamma_{\mathrm{Mg}} - N_{inner} - N_{outer}$.

Calculations of SAXS Profiles from CG Trajectories. We first backmap 10,000 randomly selected conformations to all-atom representations using Arena.[99] Because Arena only recognizes standard RNA atom names, we map the phosphate, sugar, and base beads in the CG model to P, C2', and C4 atoms, respectively. To remove steric clashes after this procedure, each structure is subjected to an energy minimization using Amber bsc0 force field with $\chi OL3$ corrections (Fig. S2A).[58,100] We then calculate SAXS profiles under the same conditions in experiments using CRYSOL with default parameters.[101]

Ion atmosphere 2D projection. Direct superposition of instantaneous ion distributions from successive trajectory snapshots provides a qualitative view of the ion atmosphere surrounding structured RNAs. However, for flexible ssRNA, such averaging leads to severe blurring that obscures spatial features of ion localization.[102] To generate an interpretable representation of the Mg^{2+} ion atmosphere, we first remove the translational and rotational motions of ssRNA by aligning each frame to the ssRNA COM and principle axes. We project the distance from every Mg^{2+} ion to its closest phosphate group using the following procedure. We define r_z as the axial distance along the RNA first principal axis, and r_{xy} is the in-plane (lateral) distance. The azimuthal angle is determined as $\theta = \arctan\frac{r_y}{r_x}$, where x and y are the components of the Mg–P vector in the xy-plane. To preserve directional information in the 2D projection, the sign of the lateral displacement is assigned according to the sign of θ, resulting in the directional in-plane distance: $r^{min}_{\mathrm{Mg^{2+}-P_{xy}}} = \mathrm{sgn}(\theta) \cdot \sqrt{x^2 + y^2}$ (Fig. 5C).

Calculations of solvent-accessible surface area (SASA). SASA is calculated using the

FreeSASA Python package.[103] In this method, a spherical probe representing the solvent molecule rolls over the solute molecule. We use the classical Lee–Richards algorithm,[104] in which the surface area is approximated by the contour of successive slices. We set the probe radius to 2.0 Å to approximate the size of a hydrated Mg^{2+} ion. The total SASA can be decomposed into contributions from the phosphate, sugar, and nucleobase groups. Lacking atomic details, SASA estimated from CG models may be biased. To access this, we benchmarked CG-derived SASA against atomistic models and found a systematic underestimation of $\approx 10\%$, likely due to surface smoothing in the CG representation (Fig. S10). Since we are interested in the relative values, comparative analysis still remains meaningful.

Calculations of the orientational correlation function. The orientational correlation function (OCF) is defined as (Eq. 11):

$$OCF = \langle \cos\theta_{ij} \rangle = \langle r_i \ \cdot \ r_j \rangle, \tag{11}$$

where r_i is the normalized bond vector connecting the ith and $(i+1)^{th}$ phosphate groups. The OCF is evaluated as a function of sequence separation $|i-j|$, which measures the correlation between local backbone orientations over increasing contour distances. The resulting OCF is averaged over all conformations in the structural ensemble to characterize the mean chain stiffness and directional persistence of ssRNA.

Statistical analysis and uncertainty estimation: Because MD trajectories are temporally correlated, individual frames were not treated as independent samples. Instead, each time series (e.g. ion counts) was divided into contiguous, non-overlapping blocks of 5,000 frames. The mean value within each block was calculated, and these block-averaged values were treated as approximately independent samples, and the effective sample size was therefore given by the number of blocks. To estimate uncertainty of the mean values and the differences between sequences, nonparametric bootstrap resampling was applied to the block-averaged data. For each comparison, 40,000 bootstrap resamples were drawn, and the resulting dis-

tribution of mean differences was used to calculate 95% confidence intervals. These intervals are reported as the primary measure of statistical significance.

Results and Discussion

Distinct Structural Ensembles of rA_{30} and rU_{30}. To access the model's accuracy in capturing ssRNA structural ensembles, we compare the simulated radii of gyration (R_g) and SAXS profiles with experiment for rA_{30} and rU_{30} at 20 °C (results for rC_{30} are in SI). Across wide concentrations of both Mg^{2+} and monovalent ions, R_g values agree well with SAXS-derived measurements, capturing ion-induced compaction (Figs. 4A, S7 and Table S5).[50,105] Overall, our model predicts that rA_{30} consistently adopts more compact conformations than rU_{30} due to stronger adenine stacking interactions, which is in agreement with experimental data.[50] Despite small R_g discrepancies, the computed SAXS profiles are in quantitative agreement with experiments (Fig. S4), and Kratky plots further highlight sequence-dependent differences in structural ensemble and collapse upon addition of Mg^{2+} (Fig. 4B). Both RNAs remain largely unstructured across the tested ion conditions; however, at 5 mM Mg^{2+}, the Kratky curve of rA_{30} bends downward, suggesting the formation of partially folded, compact conformations (Figs. S5 and S6). Such a difference between two constructs is further supported by the simulated end-to-end distances (R_{ee}), where rA_{30} exhibits shorter R_{ee} than rU_{30} (Fig. S8, Table S7).

To directly probe the ssRNA structures, we compute the OCF between phosphate groups (Fig. 4C). Changes in backbone direction reduce the OCF, which becomes negative when the vectors approach an antiparallel orientation. For rA_{30}, OCFs exhibit oscillatory behavior across ionic conditions. With added Mg^{2+}, the correlation decays rapidly, changing from positive to negative values, strongly suggesting a signature of helical structures. In contrast, rU_{30} shows monotonic decay in most conditions, suggesting a largely featureless chain. The overall shapes of our simulated OCFs are comparable to recently reported results from other

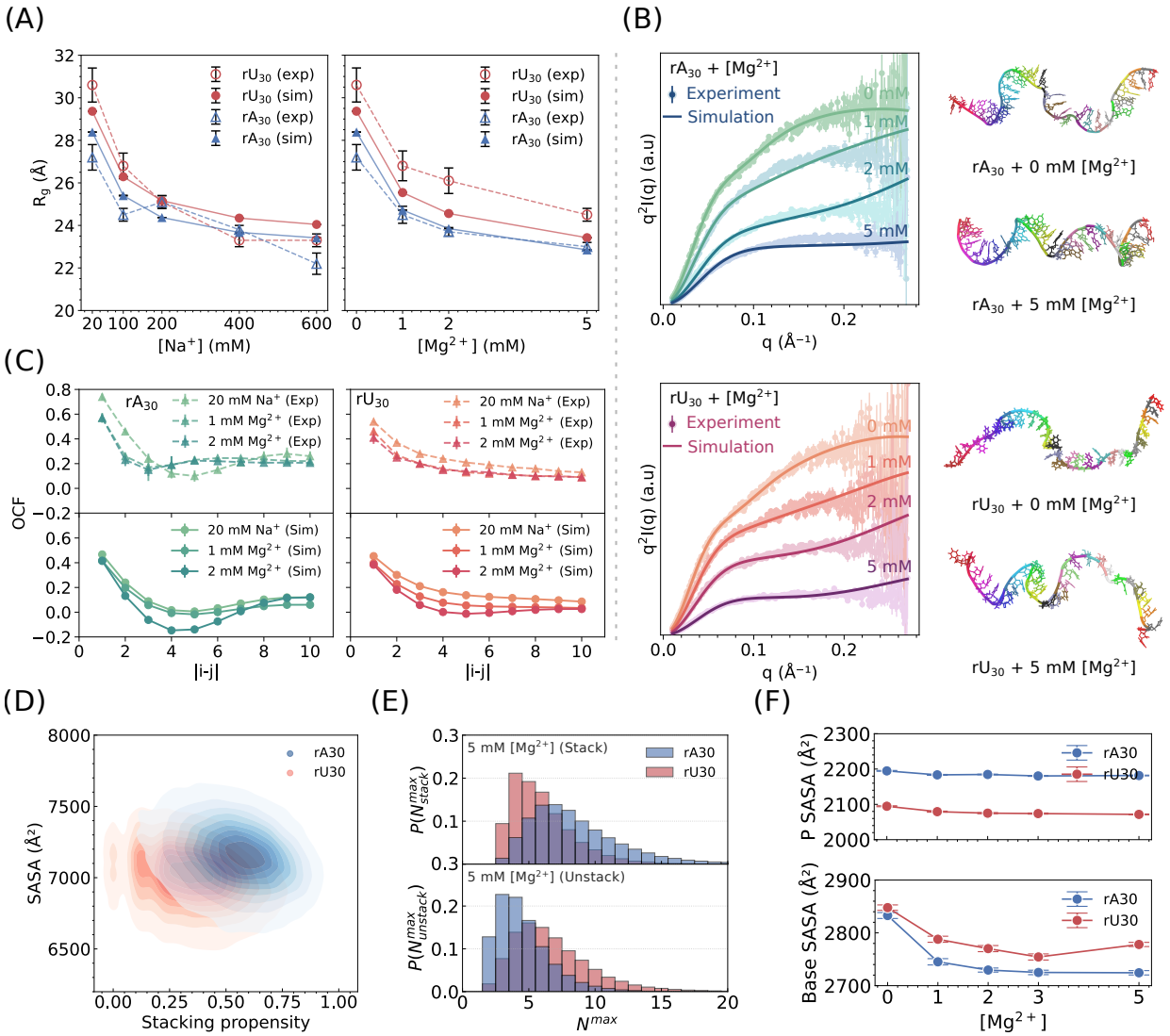

Figure 4: rA_{30} and rU_{30} populate distinct structural ensembles. **(A)** Radii of gyration from simulation plotted against SAXS-derived values for rA_{30} (blue) and rU_{30} (red) under varying Mg^{2+} and Na^{+} concentrations, showing sequence- and ion-dependent compaction. Error bars are standard error of the mean. **(B)** Comparison between simulated SAXS profiles with experiments for rA_{30} (top) and rU_{30} (bottom). On the right shown representative conformations obtained by all-atom backmapping from CG coordinates. Error bars are standard error of the mean. **(C)** Orientation correlation functions for rA_{30} (left) and rU_{30} (right) at various ion concentrations. **(D)** Solvent-accessible surface area *vs.* stacking propensity distribution of rA_{30} and rU_{30} in 5 mM Mg^{2+}. **(E)** Distribution of maximum consecutive stacking (top) and unstacking (bottom) in 20 mM Na^{+} + 5 mM Mg^{2+}. **(F)** Decomposing solvent-accessible surface area to phosphate (top) and base (bottom) contributions. Error bars represent 95% confidence intervals.

CG RNA models.[75] They are also qualitatively consistent with previous reconstruction of structural ensembles from SAXS for those sequences (Fig. S9).[50] We note that multiple distinct conformational ensembles can yield similar SAXS profiles, underscoring the need for local structural probing to fully resolve such degeneracy.

Stacking Interactions Dictate Helical Formation. To elucidate the difference in helical propensity between the two sequences, we calculate the 2D distributions of SASA and stacking propensity, defined as the fraction of nucleobases in stacked conformations (results for 20 mM Na^+ + 5 mM Mg^{2+} shown in Fig. 4D). The two distributions of rA_{30} and rU_{30} are well separated, suggesting distinct conformational ensembles. rA_{30} transiently adopts a right-handed single-stranded helical conformation (Fig. 4B), characterized by a maximum contiguous stacking length (N_{stack}^{max}) of 9 ± 4 nucleotides, whereas rU_{30} exhibits shorter stacked segments (N_{stack}^{max} of 6 ± 2) (Fig. 4E, top). As a result, the coil (unstacked) regions are shorter for rA_{30} (5 ± 2 nucleotides) than for rU_{30} (7 ± 3 nucleotides), consistent with stronger base stacking in the former (Fig. 4E, bottom). Because stacking interactions occur primarily between nearest neighbors, such helicity is expected to be only weakly cooperative.[106,107] Our results agree with single-molecule force experiments that revealed alternating helical and coil regions for poly(rA), but not for poly(rU).[108] It is also supported by crystallographic analyses of the ApApA trimer demonstrating intrinsic helical order in poly(rA).[109] Together, our simulations support a block copolymer picture of ssRNA, in which stacked and unstacked domains coexist.

These differences in stacking behavior between rA_{30} and rU_{30} directly affect solvent exposure. In particular, the helical organization of rA_{30} orients phosphate groups outward, resulting in higher phosphate SASA for rA_{30} compared to rU_{30} (Fig. 4F, top). On the other hand, nucleobase SASA is lower in rA_{30} due to stronger stacking and thus reducing base exposure (Fig. 4F, bottom). Such modulation of solvent exposure may in turn influence local ion interactions and potentially affect the recognition of single-stranded regions by regulatory proteins.[110,111]

Structure-Dependent Ion Atmosphere. The degree of ion binding to RNA can be quantified using the preferential interaction coefficient (Γ_{Mg}), which reports the excess number of ions associated with RNA relative to bulk solution.[97,98,112] Consistent with ion counting experiments,[50] our simulations reproduce the overall magnitude of Γ_{Mg} (Fig. 5A, Table S6). Experimentally, rA_{30} attracts approximately 1.5 more Mg^{2+} ions per chain than rU_{30} over the range of 0 - 3 mM Mg^{2+} and 20 mM Na^{+}, corresponding to a lower competition coefficient ($M_{1/2} = 0.9 \pm 0.1$ mM for rA_{30} vs. 1.3 ± 0.3 mM for rU_{30}). Although these values overlap within experimental uncertainty, their mean difference implies that nearly 40% higher bulk Mg^{2+} concentration is required to displace half of the monovalent ions surrounding rU_{30}.[50] This subtle sequence dependence is not captured by our simulations. However, prior work on ssDNA also found identical Γ_{Mg} for dA_{30} and dT_{30} despite pronounced differences in stacking propensity.[49,113]

To further probe the ion atmosphere in greater detail, we partition the Mg^{2+} binding into inner-sphere (direct phosphate coordination), outer-sphere (water-mediated interaction), and diffusive regions (Fig. 5B).[78,114] The majority of Mg^{2+} remains in the diffusive regime, consistent with our previous findings that unstructured RNAs favor diffuse, weakly localized ionic environments.[78] Interestingly, we find that rU_{30} has slightly more inner-sphere Mg^{2+} binding than rA_{30}, with mean counts of 3.40 ± 0.03 versus 3.09 ± 0.03, respectively. This result suggests that the overall ion atmosphere of rU_{30} is slightly more compact than rA_{30} despite both sharing the same Γ_{Mg}. Such a small difference could be amplified in longer sequences, multi-component assemblies or condensates.

To visualize sequence-dependent ion binding patterns, we align the RNA COM and principle axes, thus removing the RNA translational and rotational movement. Subsequently, we project the distance between every Mg^{2+} and its closest phosphate group onto a 2D surface (see Methods). Since rA_{30} has a small preference for helical structures, stacked phosphates align along the positive z-axis from 5' to 3', establishing a preferred direction of ion approach toward the backbone (Fig. 5C). In contrast, in the unstacked state, phosphates

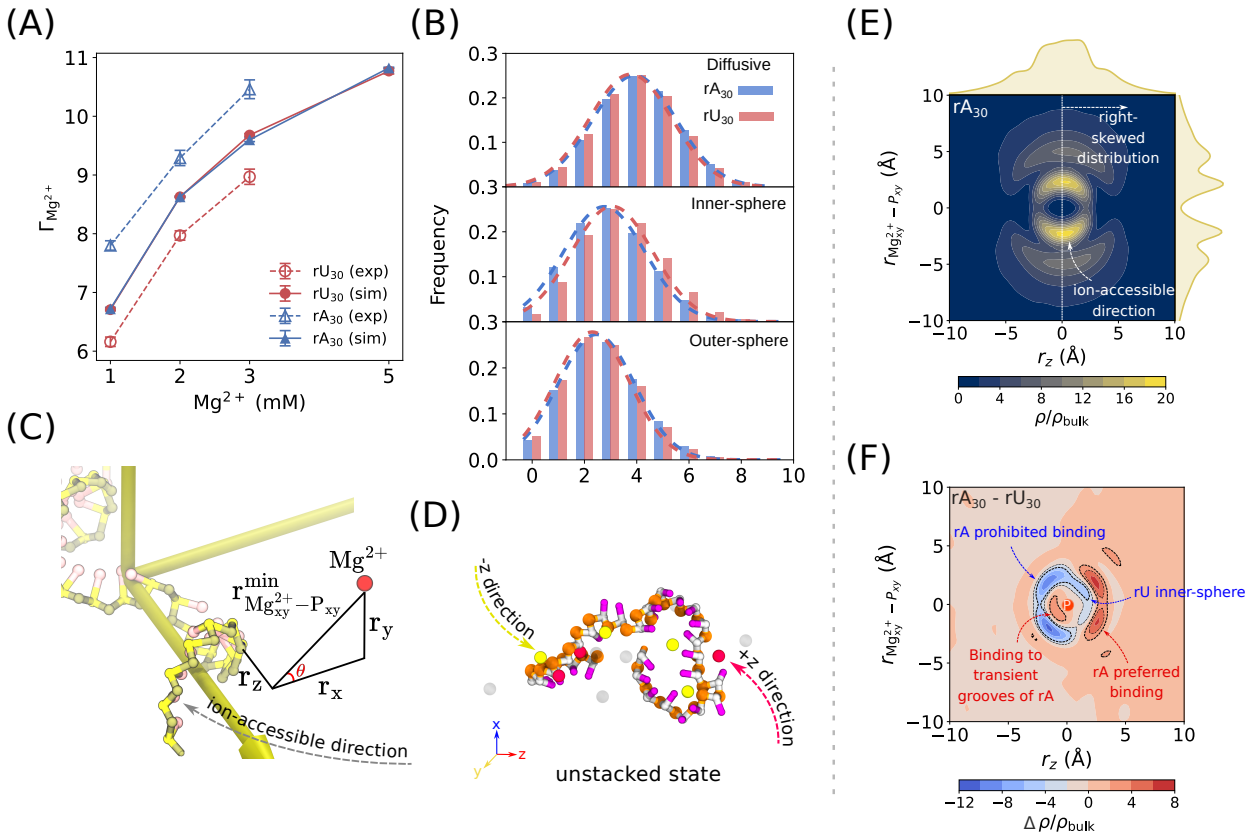

Figure 5: Sequence- and structure-dependent ion atmosphere. **(A)** Excess Mg^{2+} per chain for rA_{30} (blue) and rU_{30} (red) from simulations and buffer exchange-atomic emission spectroscopy.[50] Error bars are standard error of the mean. **(B)** Partitioning of Mg^{2+} into diffusive (top), inner-sphere (middle), and outer-sphere (bottom) binding modes. **(C)** Schematic of the alignment for ion projection, where the RNA major axis is along the z-axis. Distances $r^{min}_{Mg^{2+}-P_{xy}}$ and r_z are Mg^{2+}–phosphate separation in the xy- and z-directions, respectively; θ is the azimuthal angle. In the right-handed helical state, Mg^{2+} accessibility is restricted from a certain direction due to the presence of the sugar and base. **(D)** Schematic of the unstacked state, where Mg^{2+} can approach from both directions along the z-axis. **(E)** 2D density map of Mg^{2+} around rA_{30}, showing a right-skewed distribution consistent with the transient helical structures. The ion-accessible direction corresponds to the most populated region. **(F)** Difference density map between rA_{30} and rU_{30}. Red regions highlight preferred Mg^{2+} binding for rA_{30} in the positive z-direction and transient groove binding near the phosphate, whereas blue regions are sites more accessible in rU_{30}.

are disordered, allowing ions to approach from both the +z and −z directions (Fig. 5D). The resulting 2D density map of rA_{30} shows a slightly right-skewed distribution along the z-axis, consistent with the anisotropic ion localization expected for a transient helical structure (Figs. 5E, S19). Additional insights emerge by subtracting the rU_{30}'s distribution from rA_{30}'s (Fig. 5F): a distinct region of enhanced Mg^{2+} density appears along the positive z-axis, indicating a site where rA_{30} preferentially binds ions. Conversely, the region in the corresponding negative z-axis is depleted for rA_{30}, suggesting that this binding site is more

accessible in rU_{30}. Furthermore, localized hotspots of density indicate Mg^{2+} association with the transient helical grooves of rA_{30}, reflecting its stacked, groove-forming structure that is absent in the largely unstacked rU_{30} ensemble. In other words, the chirality of the RNA imposes a chiral organization on its counterions. This phenomenon is analogous to how water molecules form a chiral hydration structure around duplex DNA, aligning in helical patterns along the major and minor grooves of the double helix.[115–118] Together, these results demonstrate that Mg^{2+} ions neutralize ssRNA by organizing to form a complex ion atmosphere shaped by the RNA's 3D organization. The ion atmosphere is therefore an extension of the RNA's structure, inheriting its helical grooves, directional geometry, and chirality rather than forming a uniform shell.[119] Such coupling between RNA shape and ion distribution underscores that ions "sense" the helix's handedness and stabilize the structure in an asymmetric fashion, which has important implications for RNA folding and molecular recognition.

Thermal Compaction of Homopolymeric ssRNA. The newly developed PMF allows us to study how ions modulate RNA conformations at various temperatures. Remarkably, we found that R_g values of ssRNAs display non-monotonic behaviors when the temperature increases from 0 °C to 100 °C (Fig. 6B). Even in the absence of Mg^{2+}, rA_{30} exhibits a relatively long expansion phase, reaching a maximum at $T_{\max} = 76$ °C before undergoing mild collapse, whereas rU_{30} shows limited expansion and collapses earlier at $T_{\max} = 48$ °C. Introduction of 1 mM Mg^{2+} sharply lowers $T_{\max}$ (to 59 °C for rA_{30} and 15 °C for rU_{30}), with little additional shift up to 5 mM.

To further dissect the conformational ensembles of ssRNAs across temperatures, we examined the 2D distribution of SASA and stacking propensity at various ionic conditions. As temperature increases, all RNAs exhibit a shift towards lower stacking propensity and higher SASA. This shift occurs more rapidly for rA_{30} than for rU_{30} (Figs. S12). Consistently, projection of the higher-dimensional space comprising of R_g, R_{ee}, SASA, stacking potential and Mg–P interaction energies onto two dimensions using t-SNE reveals the same trend

(Figs. S11, S13). For rA_{30}, pronounced helical signatures are evident at 0 °C and 20 °C, characterized by oscillatory OCFs that alternate between negative and positive values. These helical correlations vanish at high temperatures, indicating loss of ordered stacking. In contrast, rU_{30} displays only weak helicity even at 0 °C, and its OCFs decay monotonically at all temperatures, suggesting that uracil-rich structures respond more weakly to thermal perturbation (Fig. 6D). Compared with their corresponding dinucleotides, both rA_{30} and rU_{30} unstack more rapidly upon heating (Fig. 6E). Structural ensembles[120] of rA_{30} highlight drastic changes across temperatures: stacked and compact conformations dominate at low temperatures, expanded intermediates emerge at moderate temperatures, whereas collapsed structures prevail at high temperatures (Fig. 6F).

Similar temperature-induced collapse has been observed in all-atom simulations of poly phosphate.[52] Light scattering experiments on poly(rA) also found it collapsing when temperature increases, where stacking disruption was proposed as the main mechanism.[121] However, disruption of base stacking is expected to render rA_{30} indistinguishable from rU_{30}, leading to a larger R_g. Consistent with this expectation, at high temperatures where the stacking fractions of both sequences converge to similar values (Fig. 6E), we observe that their R_g become identical, and the sequence dependence disappears (Fig. 6B).

To understand why such collapses occur, we turn our attention to ion-RNA interactions as hinted by the PMF. It has been known that the binding of divalent ions to phosphate groups is driven by entropy, thus increasing temperature leads to a more stable binding.[122,123] In our framework, temperature affects the ion binding through two coupled terms: (i) the inverse thermal factor $\beta = 1/k_B T$ in the RISM theory and when calculating $W(r)$ from $g_{Mg-P}(r)$, and (ii) the dielectric constant of water, $\epsilon_r(T)$, which decreases at elevated temperature and thereby effectively strengthens electrostatic interactions. Together, those effects stabilize both inner- and outer-sphere minima of the Mg^{2+}–phosphate PMF at high temperatures (Fig. 3). We note that this enhanced affinity has an entropic origin, arising from the release of ordered water molecules and competing counterions into the bulk solution. In particular,

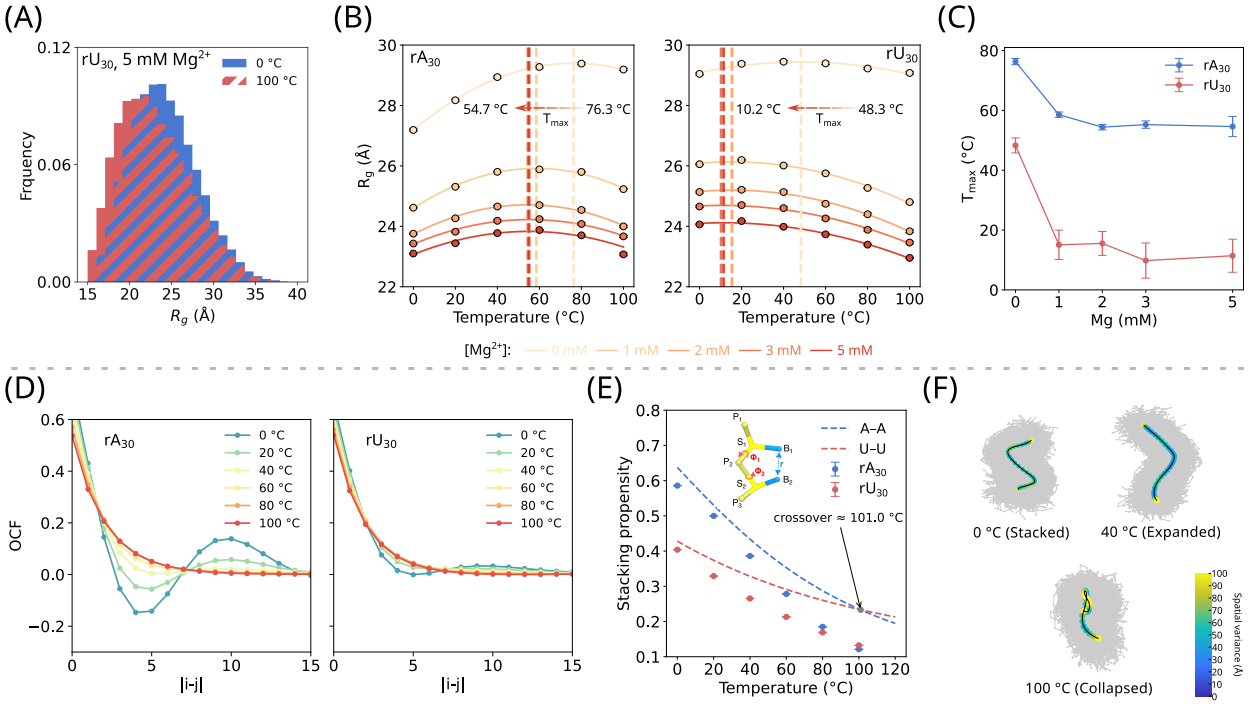

Figure 6: ssRNA collapses at high temperature. **(A)** Distribution of R_g at 0 °C (blue) and 100 °C (red) of rU_{30} in 5 mM Mg^{2+}. **(B)** R_g of rA_{30} (left) and rU_{30} (right) as a function of temperature in 0-5 mM Mg^{2+}. Vertical dashed lines denote $T_{\max}$, the temperature of maximal expansion, which marks the transition from chain expansion to collapse. Error bars are standard errors of the mean, with the maximum value being 0.04 Å across all conditions, thus smaller than the markers. Numerical values are reported in Table S8 and S9. **(C)** Dependence of T_{max} on Mg^{2+} concentration for rA_{30} (blue) and rU_{30} (red). Error bars are standard error of the mean. **(D)** Orientational correlation functions from 0 °C to 100 °C for rA_{30} (left) and rU_{30} (right). **(E)** Stacking propensity decreases with temperature for rA_{30} and rU_{30}. Dotted lines show prediction from the dinucleotide model, which underestimates the accelerated decay observed in long sequences. Error bars are standard error of the mean. **(F)** Representative conformational ensemble of rA_{30} at 0 °C, 40 °C, and 100 °C.

the temperature dependence of the dielectric constant of water gives rise to a substantial entropic contribution to the electrostatic interaction used in CG modeling, as illustrated in a recent work.[124]

We rationalize the non-monotonic behavior of R_g by considering the coupled effects of electrostatics and base stacking. The Bjerrum length $l_B = \frac{e^2}{4\pi\epsilon_0\epsilon_r(T)k_BT}$ (where ϵ_r is the temperature-dependent dielectric constant of water) sets the strength of electrostatic interactions. With increasing temperature, $\epsilon_r T$ decreases, resulting in an overall lengthening of l_B (Fig. S14A). Consequently, electrostatic interactions become stronger at higher temperatures, promoting enhanced counterion condensation on the phosphate backbone (Fig.

S14B). The resulting effective P–P repulsion thus exhibits a non-monotonic temperature dependence: it initially increases as the electrostatic interactions strengthen but subsequently weakens once extensive counterion adsorption more effectively neutralizes the backbone charges (Fig. S14D). In the presence of Mg^{2+}, such effect is much more pronounced because of its stronger affinity towards phosphate groups at elevated temperatures (Fig. 3), which has been demonstrated in all-atom simulations.[52,66,75]

Additionally, base-base stacking further modulates this behavior in a sequence-dependent manner. Stacking propensity decreases monotonically with temperature (Fig. 6E), so the thermal disruption of stacking interactions drives an initial expansion of RNA. The overall temperature profile of R_g therefore reflects a balance between stacking and electrostatic effects: R_g first increases as stacking weakens, then subsequently decreases as counterion condensation dominates at higher temperatures. Adenines stack more favorably than uracils, explaining why rA_{30} expands substantially upon heating, whereas rU_{30} with weak stacking shows minimal expansion. Interestingly, Mg^{2+} affects stacking interactions minimally (Fig. S15). Therefore, the pronounced dependence of $T_{\max}$ on Mg^{2+} arises mainly because divalent cations are far more effective at neutralizing RNA charge than monovalent ions, altering the electrostatic balance that governs the transition. This mechanism also explains the observed saturation at high Mg^{2+} concentrations.

We emphasize that structured or partially folded RNAs generally display monotonic expansion with increasing temperature.[125] One key difference between the sequences studied here and structured RNAs is the lack of a stable tertiary fold in unstructured RNAs. As a result, those RNAs do not undergo unfolding at high temperature, which often correlates to a large expansion in size, as seen in folded domains. The collapse at high temperatures observed here and elsewhere[52,121] does not correspond to formation of folded or native-like structure, but it reflects polymer-level reorganization driven by enhanced ion condensation. In the case of folded structures, this ion-driven collapse is masked by a much larger expansion due to RNA unfolding. It is therefore desirable to separate the contribution of ion-facilitated

interaction from RNA unfolding using the simple systems studied here.

Reorganization of the Ion Atmosphere at Elevated Temperature. To quantify how ions induce such collapses, we calculate Γ_{Mg} at various temperatures. Across all conditions, Γ_{Mg} increases slightly with temperature (Fig. 7A, Tables S10, S11), indicating enhanced Mg^{2+} absorption into the RNA ion atmosphere. Our result is consistent with the strengthening of Mg^{2+}-P and thus Mg^{2+}-RNA interactions at high temperatures.[52,66,75,122,123] Strikingly, our simulations unveil a clear redistribution of Mg^{2+} from the diffusive to the inner-sphere populations as temperature rises, while the outer-sphere contribution remains largely unchanged (Fig. 7B). Quantitatively, the number of inner-sphere ions increases by nearly 1.5 per RNA, accompanied by a corresponding decrease of about 1 ion in the diffusive population. At elevated temperatures, the inner-sphere ions outnumber the diffusive counterparts, signaling a temperature-driven collapse of the Mg^{2+} atmosphere surrounding the RNA (Fig. S18). 2D ion density maps comparing between 0 °C and 100 °C vividly illustrate this rearrangement. For rA_{30}, the diffusive layer becomes markedly depleted as ions migrate inward to form direct, inner-sphere contacts with phosphate groups. The concurrent loss of base stacking further facilitates this redistribution. rU_{30} also exhibits a similar shift (Fig. 7C), but the magnitude is much less pronounced, consistent with its weaker stacking propensity (Fig. 7D).

This temperature-driven transition therefore reflects an entropically favored reorganization of the ion atmosphere. Formation of inner-sphere contacts requires partial dehydration of ${Mg(H_2O)_6}^{2+}$, an energetically costly process that releases tightly bound water molecules into bulk solvent. The resulting gain in translational and rotational entropy of released water grows with temperature, progressively offsetting the dehydration enthalpy and thus stabilizing direct Mg^{2+}–phosphate coordination. Such entropy-driven binding and assembly processes have also been found in the ion-induced assembly of polyphosphates,[52] RNA,[52,66,75] and polyelectrolyte coacervation.[124,126,127] In addition, our findings have implications for thermoresponsive behavior of RNA condensates. The expansion of ssRNA at

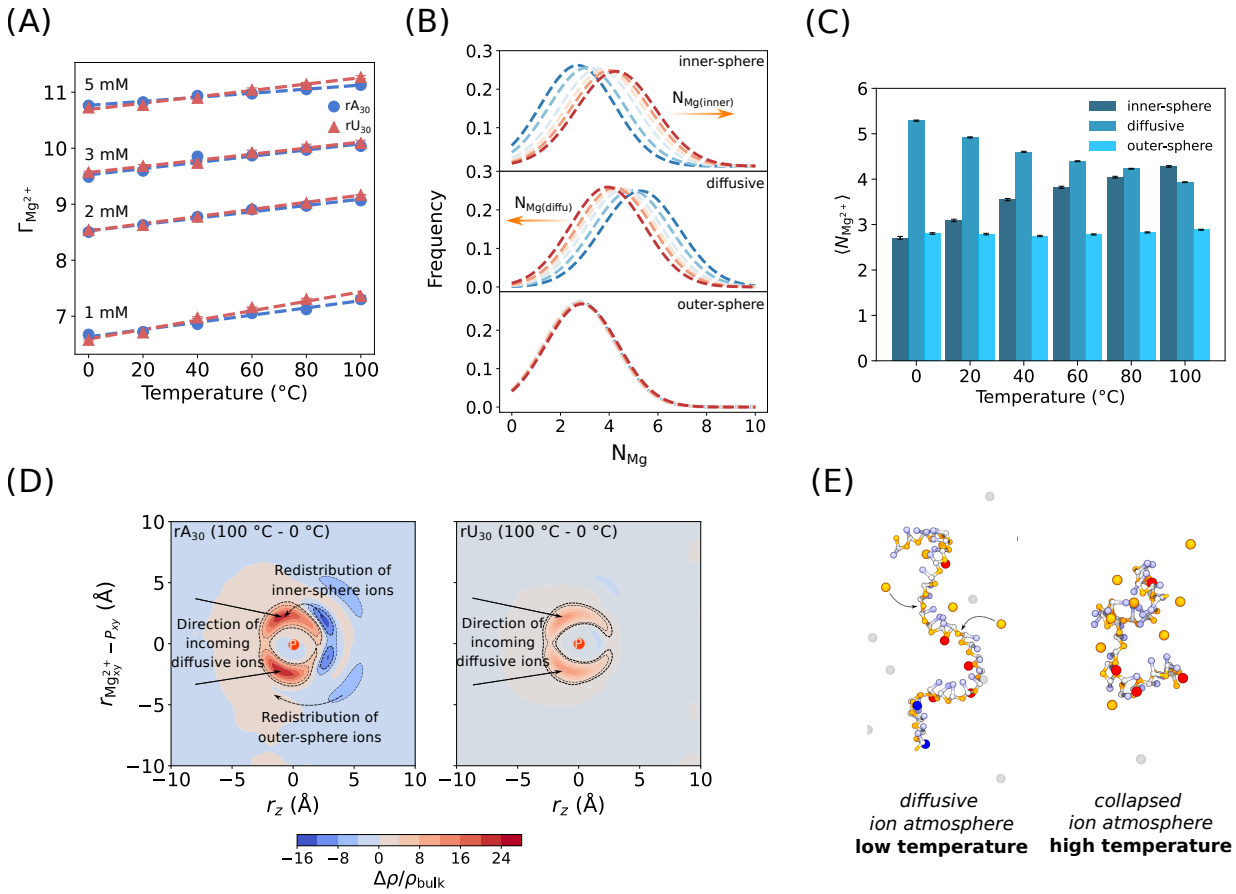

Figure 7: Ion reorganization at high temperature. **(A)** Preferential interaction coefficient for Mg^{2+} increases linearly with temperature for both rA_{30} (blue) and rU_{30} (red) at all Mg^{2+} concentrations. Error bars are standard error of the mean. **(B)** Partitioning of rA_{30} ion atmosphere into inner-sphere (top), diffusive (middle), and outer-sphere (bottom) bindings. Increasing temperature drives ions from the diffusive to the inner-sphere regions. **(C)** Ion atmosphere composition from 0 to 100 °C of rU_{30} in 5 mM Mg^{2+}. Error bars represent 95% confidence intervals. **(D)** Difference in 2D ion density map (100 °C - 0 °C). **Left:** rA_{30} shows heating reorganizes diffusive ions towards inner-sphere binding, while outer-sphere and inner-sphere ions shift with the loss of stacking. **Right:** Reorganization is much weaker for rU_{30} than in rA_{30} due to smaller changes of stacking during heating. **(E)** Schematic illustration of diffusive-to-inner-sphere ion migration underlying temperature-induced collapse of the ion atmosphere.

relatively low temperature followed by collapse at high temperature, as observed here, is a hallmark of lower critical solution temperature (LCST)-type phase separation.[52,128–130] The strong coupling between coil-globule transitions and Mg^{2+} binding uncovered in this study may provide a microscopic basis for LCST-driven RNA condensation, and help explain how RNAs maintain structural integrity and function across a wide thermal range, including in thermophilic environments,[131–134] or cold-induced RNA misfolding transitions.[135]

Conclusion

Our work establishes a molecular framework for understanding how temperature and ions together shape the structural ensemble of ssRNAs. Using CG simulations, we quantitatively reproduce experimental SAXS profiles (and R_g) across a wide range of ion concentrations. Although ssRNAs are highly flexible and lack stable secondary structure, we show that base-stacking interactions govern the degree of right-handed helix formation, with rA_{30} forming the most persistent helical structure. Remarkably, while all sequences attract comparable numbers of ions, rU_{30} shows a slight preference for inner-sphere coordination, indicating sequence-dependent ion binding propensities. In contrast, the ion atmosphere around rA_{30} exhibits a small but detectable degree of chirality. These modest variations, though minor at the single-chain level, could enable binding partners to "sense" sequence identity through electrostatic or chiral recognition and are likely to be amplified in multichain contexts such as RNA condensate formation.

By incorporating a novel temperature-dependent Mg^{2+}-phosphate potential into the simulations, we are able to illustrate the interplay between RNA structural ensemble and its ion atmosphere across temperatures. Our simulations reveal a sequence-specific collapse of RNAs at high temperature due to differences in base-stacking propensity. Each sequence exhibits a non-monotonic compaction, with distinct expansion temperature maxima that shift downward in the presence of Mg^{2+}, underscoring the electrostatic origin of the transition. At high temperatures, transient helical structures are lost, rendering all sequences being equal. We show that Mg^{2+} binding increases slightly with temperature, consistent with the entropic nature of ion binding.[124,136] As temperature rises, ions migrate from diffuse to inner-sphere regions, directly linking RNA compaction to dehydration and tighter phosphate coordination. Together, these findings highlight that RNA ion atmosphere is not a passive screening layer but a dynamic, sequence-encoded extension of the RNA structure itself. By integrating counterion condensation, base stacking, and temperature-driven collapse within a unified framework, our study provides a molecular basis for understanding how simple

RNA sequences undergo ion-mediated structural transitions and phase behaviors.

Acknowledgments

We thank Peter Eastman for valuable discussions regarding the implementation of simulations in OpenMM.

Author Contributions Statement

H.Z. implemented the model and the computational framework, analyzed the data, and took the lead in writing the manuscript. H.M. assisted with data analysis and model validation. H.T.N. supervised the project, guided data interpretation, and revised the manuscript.

Funding

We gratefully acknowledge financial support from the University at Buffalo to H.T.N.. Computational resources were provided by the Center for Computational Research at the University at Buffalo.

References

(1) Ding, Y.; Tang, Y.; Kwok, C. K.; Zhang, Y.; Bevilacqua, P. C.; Assmann, S. M. In vivo genome-wide profiling of RNA secondary structure reveals novel regulatory features. *Nature* **2014**, *505*, 696–700.

(2) Wan, Y.; Kertesz, M.; Spitale, R. C.; Segal, E.; Chang, H. Y. Understanding the transcriptome through RNA structure. *Nat. Rev. Genet.* **2011**, *12*, 641–655.

(3) Li, X.; Quon, G.; Lipshitz, H. D.; Morris, Q. Predicting in vivo binding sites of RNA-binding proteins using mRNA secondary structure. *RNA* **2010**, *16*, 1096.

(4) Garneau, N. L.; Wilusz, J.; Wilusz, C. J. The highways and byways of mRNA decay. *Nat. Rev. Mol. Cell. Biol.* **2007**, *8*, 113–126.

(5) Warf, M. B.; Berglund, J. A. Role of RNA structure in regulating pre-mRNA splicing. *Trends Biochem. Sci* **2010**, *35*, 169–178.

(6) Martin, K. C.; Ephrussi, A. mRNA Localization: Gene Expression in the Spatial Dimension. *Cell* **2009**, *136*, 719–730.

(7) Vicens, Q.; Kieft, J. S. Thoughts on how to think (and talk) about RNA structure. *Proc. Natl. Acad. Sci. U.S.A.* **2022**, *119*, e2112677119.

(8) Thirumalai, D.; Hyeon, C. RNA and Protein Folding: Common Themes and Variations. *Biochemistry* **2005**, *44*, 4957–4970.

(9) Bevilacqua, P. C.; Ritchey, L. E.; Su, Z.; Assmann, S. M. Genome-Wide Analysis of RNA Secondary Structure. *Annu. Rev. Genet.* **2016**, *50*, 235–266.

(10) Cech, T. R.; Bass, B. L. Biological catalysis by RNA. *Annu. Rev. Biochem.* **1986**, *55*, 599–629.

(11) Draper, D. E. A guide to ions and RNA structure. *RNA* **2004**, *10*, 335.

(12) Römer, R.; Hach, R. tRNA Conformation and Magnesium Binding. *Eur. J. Biochem.* **1975**, *55*, 271–284.

(13) Stein, A.; Crothers, D. M. Conformational changes of transfer RNA. The role of magnesium(II). *Biochemistry* **1976**, *15*, 160–168.

(14) Stein, A.; Crothers, D. M. Equilibrium binding of magnesium(II) by Escherichia coli tRNAfMet. *Biochemistry* **1976**, *15*, 157–160.

(15) Sanchez de Groot, N.; Armaos, A.; Graña-Montes, R.; Alriquet, M.; Calloni, G.; Vabulas, R. M.; Tartaglia, G. G. RNA structure drives interaction with proteins. *Nat. Commun.* **2019**, *10*, 3246.

(16) Ganser, L. R.; Kelly, M. L.; Herschlag, D.; Al-Hashimi, H. M. The roles of structural dynamics in the cellular functions of RNAs. *Nat. Rev. Mol. Cell. Biol.* **2019**, *20*, 474–489.

(17) Cantara, W. A.; Crain, P. F.; Rozenski, J.; McCloskey, J. A.; Harris, K. A.; Zhang, X.; Vendeix, F.

A. P.; Fabris, D.; Agris, P. F. The RNA modification database, RNAMDB: 2011 update. *Nucleic Acids Res.* **2011**, *39*, D195–D201.

(18) Delaunay, S.; Helm, M.; Frye, M. RNA modifications in physiology and disease: towards clinical applications. *Nat. Rev. Genet.* **2024**, *25*, 104–122.

(19) Cappannini, A.; Ray, A.; Purta, E.; Mukherjee, S.; Boccaletto, P.; Moafinejad, S. N.; Lechner, A.; Barchet, C.; Klaholz, B.; Stefaniak, F.; Bujnicki, J. M. MODOMICS: a database of RNA modifications and related information. 2023 update. *Nucleic Acids Res.* **2024**, *52*, D239–D244.

(20) Lewis, C. J. T.; Pan, T.; Kalsotra, A. RNA modifications and structures cooperate to guide RNA–protein interactions. *Nat. Rev. Mol. Cell. Biol.* **2017**, *18*, 202–210.

(21) Munroe, D.; Jacobson, A. mRNA Poly (A) Tail, a 3 Enhancer of Translational Initiation. *Mol. Cell. Biol.* **1990**, *10*, 3441–3455.

(22) Decker, C. J.; Parker, R. A turnover pathway for both stable and unstable mRNAs in yeast: evidence for a requirement for deadenylation. *Genes Dev.* **1993**, *7*, 1632–1643.

(23) Wang, Z.; Day, N.; Trifillis, P.; Kiledjian, M. An mRNA Stability Complex Functions with Poly(A)-Binding Protein To Stabilize mRNA In Vitro. *Mol. Cell. Biol.* **1999**, *19*, 4552–4560.

(24) Chen, Z.; Li, Y.; Krug, R. M. Influenza A virus NS1 protein targetspoly(A)-binding protein II of the cellular 3-end processing machinery. *EMBO J.* **1999**, *18*, 2273–2283.

(25) Tian, B.; Hu, J.; Zhang, H.; Lutz, C. S. A large-scale analysis of mRNA polyadenylation of human and mouse genes. *Nucleic Acids Res.* **2005**, *33*, 201–212.

(26) Craig, A. W. B.; Haghighat, A.; Yu, A. T. K.; Sonenberg, N. Interaction of polyadenylate-binding protein with the eIF4G homologue PAIP enhances translation. *Nature* **1998**, *392*, 520–523.

(27) Hall, T. M. T. Poly(A) tail synthesis and regulation: recent structural insights. *Curr. Opin. Struct. Biol.* **2002**, *12*, 82–88.

(28) Makeyev, A. V.; Liebhaber, S. A. The poly(C)-binding proteins: a multiplicity of functions and a search for mechanisms. *RNA* **2002**, *8*, 265.

(29) Eliseeva, I. A.; Lyabin, D. N.; Ovchinnikov, L. P. Poly(A)-binding proteins: Structure, domain organization, and activity regulation. *Biochemistry (Mosc)* **2013**, *78*, 1377–1391.

(30) Wigington, C. P.; Williams, K. R.; Meers, M. P.; Bassell, G. J.; Corbett, A. H. Poly(A) RNA-binding proteins and polyadenosine RNA: new members and novel functions. *WIREs RNA* **2014**, *5*, 601–622.

(31) Denman, R. B. Déjà vu all over again: FMRP binds U-rich target mRNAs. *Biochem. Biophys. Res. Commun.* **2003**, *310*, 1–7.

(32) Fresco, J. R.; Doty, P. Polynucleotides. I. Molecular Properties and Configurations of Polyriboadenylic Acid in Solution. *J. Am. Chem. Soc.* **1957**, *79*, 3928–3929.

(33) Dewey, T. G.; Turner, D. H. Laser temperature-jump study of stacking in adenylic acid polymers. *Biochemistry* **1979**, *18*, 5757–5762.

(34) Leng, M.; Felsenfeld, G. A study of polyadenylic acid at neutral pH. *J. Mol. Biol.* **1966**, *15*, 455–466.

(35) Brahms, J. Optical activity and the conformation of polynucleotide models of nucleic acids. *J. Mol. Biol.* **1965**, *11*, 785–801.

(36) Adler, A. J.; Grossman, L.; Fasman, G. D. Polyriboadenylic and polydeoxyriboadenylic acids. Optical rotatory studies of pH-dependent conformations and their relative stability. *Biochemistry* **1969**, *8*, 3846–3859.

(37) Warshaw, M. M.; Bush, C.; Tinoco, I. The optical rotatory dispersion of adenylyl (3–5) adenosine and its significance for polynucleotide rotations. *Biochem. Biophys. Res. Commun.* **1965**, *18*, 633–638.

(38) Poland, D.; Vournakis, J. N.; Scheraga, H. A. Cooperative interactions in single-strand oligomers of adenylic acid. *Biopolymers* **1966**, *4*, 223–235.

(39) Brahms, J.; Mommaerts, W. F. H. M. A study of conformation of nucleic acids in solution by means of circular dichroism. *J. Mol. Biol.* **1964**, *10*, 73–88.

(40) Kondo, N. S.; Fang, K. N.; Miller, P. S.; Ts'o, P. O. Influence of the furanose on the conformation of adenine dinucleoside monophosphates in solution. *Biochemistry* **1972**, *11*, 1991–2003.

(41) Broido, M. S.; Kearns, D. R. Proton NMR evidence for a left-handed helical structure of poly(ribocytidylic acid) in neutral solution. *J. Am. Chem. Soc.* **1982**, *104*, 5207–5216.

(42) Holcomb, D. N.; Tinoco, I. Conformation of polyriboadenylic acid: pH and temperature dependence. *Biopolymers* **1965**, *3*, 121–133.

(43) Arnott, S.; Chandrasekaran, R.; Leslie, A. G. Structure of the single-stranded polyribonucleotide polycytidylic acid. *J. Mol. Biol.* **1976**, *106*, 735–748.

(44) Krakauer, H. The binding of Mg++ ions to polyadenylate, polyuridylate, and their complexes. *Biopolymers* **1971**, *10*, 2459–2490.

(45) Gellert, M.; Lipsett, M. N.; Davies, D. R. Helix formation by guanylic acid. *Proc. Natl. Acad. Sci. U.S.A.* **1962**, *48*, 2013–2018.

(46) Pörschke, D. The mode of Mg++ binding to oligonucleotides. Inner sphere complexes as markers for recognition? *Nucleic Acids Res.* **1979**, *6*, 883–898.

(47) Draper, D. E. RNA Folding: Thermodynamic and Molecular Descriptions of the Roles of Ions. *Biophys. J.* **2008**, *95*, 5489–5495.

(48) Hideki Aizaki, J. L. G. Nanoimaging of ssRNA: Genome Architecture of the Hepatitis C Virus Revealed by Atomic Force Microscopy. *J. Nanomed. Nanotechol.* **2011**, *s5*.

(49) Plumridge, A.; Meisburger, S. P.; Pollack, L. Visualizing single-stranded nucleic acids in solution. *Nucleic Acids Res.* **2017**, *45*, e66.

(50) Plumridge, A.; Andresen, K.; Pollack, L. Visualizing Disordered Single-Stranded RNA: Connecting Sequence, Structure, and Electrostatics. *J. Am. Chem. Soc.* **2020**, *142*, 109–119.

(51) Woodson, S. A. Metal ions and RNA folding: a highly charged topic with a dynamic future. *Curr Opin Chem Biol* **2005**, *9*, 104–109.

(52) Wadsworth, G. M.; Zahurancik, W. J.; Zeng, X.; Pullara, P.; Lai, L. B.; Sidharthan, V.; Pappu, R. V.; Gopalan, V.; Banerjee, P. R. RNAs undergo phase transitions with lower critical solution temperatures. *Nat. Chem.* **2023**, *15*, 1693–1704.

(53) Aumiller, W. M.; Keating, C. D. Phosphorylation-mediated RNA/peptide complex coacervation as a model for intracellular liquid organelles. *Nat. Chem.* **2016**, *8*, 129–137.

(54) Van Treeck, B.; Protter, D. S. W.; Matheny, T.; Khong, A.; Link, C. D.; Parker, R. RNA self-assembly contributes to stress granule formation and defining the stress granule transcriptome. *Proc. Natl. Acad. Sci. U.S.A.* **2018**, *115*, 2734–2739.

(55) Boeynaems, S.; Holehouse, A. S.; Weinhardt, V.; Kovacs, D.; Van Lindt, J.; Larabell, C.; Van Den Bosch, L.; Das, R.; Tompa, P. S.; Pappu, R. V.; Gitler, A. D. Spontaneous driving forces give rise to protein-RNA condensates with coexisting phases and complex material properties. *Proc. Natl. Acad. Sci. U.S.A.* **2019**, *116*, 7889–7898.

(56) Wang, T.; Hu, Q.; Fronhofer, S.; Pollack, L. Nucleotide-Specific RNA Conformations and Dynamics as Precursors to Ribonucleoprotein Condensates. *J. Am. Chem. Soc.* **2025**, *147*, 36146–36161.

(57) Tom, J. K. A.; Onuchic, P. L.; Deniz, A. A. Short PolyA RNA Homopolymers Undergo Mg2+-Mediated Kinetically Arrested Condensation. *J. Phys. Chem. B* **2022**, *126*, 9715–9725.

(58) Zgarbová, M.; Otyepka, M.; Šponer, J.; Mládek, A.; Banáš, P.; Cheatham, T. E. I.; Jurečka, P. Refinement of the Cornell et al. Nucleic Acids Force Field Based on Reference Quantum Chemical Calculations of Glycosidic Torsion Profiles. *J. Chem. Theory Comput.* **2011**, *7*, 2886–2902.

(59) Tubbs, J. D.; Condon, D. E.; Kennedy, S. D.; Hauser, M.; Bevilacqua, P. C.; Turner, D. H. The Nuclear Magnetic Resonance of CCCC RNA Reveals a Right-Handed Helix, and Revised Parameters for AMBER Force Field Torsions Improve Structural Predictions from Molecular Dynamics. *Biochemistry* **2013**, *52*, 996–1010.

(60) Condon, D. E.; Kennedy, S. D.; Mort, B. C.; Kierzek, R.; Yildirim, I.; Turner, D. H. Stacking in RNA: NMR of Four Tetramers Benchmark Molecular Dynamics. *J. Chem. Theory Comput.* **2015**, *11*, 2729–2742.

(61) Schrodt, M. V.; Andrews, C. T.; Elcock, A. H. Large-Scale Analysis of 48 DNA and 48 RNA Tetranu-

cleotides Studied by 1 µs Explicit-Solvent Molecular Dynamics Simulations. *J. Chem. Theory Comput.* **2015**, *11*, 5906–5917.

(62) Bergonzo, C.; Henriksen, N. M.; Roe, D. R.; Cheatham, T. E. Highly sampled tetranucleotide and tetraloop motifs enable evaluation of common RNA force fields. *RNA* **2015**, *21*, 1578–1590.

(63) Mlýnský, V.; Kührová, P.; Pykal, M.; Krepl, M.; Stadlbauer, P.; Otyepka, M.; Banáš, P.; Šponer, J. Can We Ever Develop an Ideal RNA Force Field? Lessons Learned from Simulations of the UUCG RNA Tetraloop and Other Systems. *J. Chem. Theory Comput.* **2025**, *21*, 4183–4202.

(64) Zhang, C.; Lu, C.; Jing, Z.; Wu, C.; Piquemal, J.-P.; Ponder, J. W.; Ren, P. AMOEBA Polarizable Atomic Multipole Force Field for Nucleic Acids. *J. Chem. Theory Comput.* **2018**, *14*, 2084–2108.

(65) Tan, D.; Piana, S.; Dirks, R. M.; Shaw, D. E. RNA force field with accuracy comparable to state-of-the-art protein force fields. *Proc. Natl. Acad. Sci. U.S.A.* **2018**, *115*, E1346–E1355.

(66) Ramachandran, V.; Potoyan, D. A. Molecular drivers of RNA phase separation. *Proc. Natl. Acad. Sci. U.S.A.* **2025**, *122*, e2511348122.

(67) Cruz-León, S.; Grotz, K. K.; Schwierz, N. Extended magnesium and calcium force field parameters for accurate ion–nucleic acid interactions in biomolecular simulations. *J. Chem. Phys.* **2021**, *154*, 171102.

(68) Koca Fındık, B.; Jafari, M.; Song, L. F.; Li, Z.; Aviyente, V.; Merz, K. M. J. Binding of Phosphate Species to Ca2+ and Mg2+ in Aqueous Solution. *J. Chem. Theory Comput.* **2024**, *20*, 4298–4307.

(69) Boniecki, M. J.; Lach, G.; Dawson, W. K.; Tomala, K.; Lukasz, P.; Soltysinski, T.; Rother, K. M.; Bujnicki, J. M. SimRNA: a coarse-grained method for RNA folding simulations and 3D structure prediction. *Nucleic Acids Res.* **2016**, *44*, e63.

(70) Thirumalai, D.; Hori, N.; Nguyen, H. T. Minimal models for RNA simulations. *Curr. Opin. Struct. Biol.* **2025**, *93*, 103107.

(71) Šulc, P.; Romano, F.; Ouldridge, T. E.; Doye, J. P. K.; Louis, A. A. A nucleotide-level coarse-grained model of RNA. *J. Chem. Phys.* **2014**, *140*, 235102.

(72) Li, J.; Zhang, S.; Zhang, D.; Chen, S.-J. Vfold-Pipeline: a web server for RNA 3D structure prediction from sequences. *Bioinformatics* **2022**, *38*, 4042–4043.

(73) Uusitalo, J. J.; Ingólfsson, H. I.; Marrink, S. J.; Faustino, I. Martini Coarse-Grained Force Field: Extension to RNA. *Biophys. J.* **2017**, *113*, 246–256.

(74) Yasuda, I.; von Bülow, S.; Tesei, G.; Yamamoto, E.; Yasuoka, K.; Lindorff-Larsen, K. Coarse-Grained Model of Disordered RNA for Simulations of Biomolecular Condensates. *J. Chem. Theory Comput.* **2025**, *21*, 2766–2779.

(75) Li, S.; Chen, J. Driving forces of RNA condensation revealed through coarse-grained modeling with explicit Mg2+. *Proc. Natl. Acad. Sci. U.S.A.* **2025**, *122*, e2504583122.

(76) Joseph, J. A.; Reinhardt, A.; Aguirre, A.; Chew, P. Y.; Russell, K. O.; Espinosa, J. R.; Garaizar, A.; Collepardo-Guevara, R. Physics-driven coarse-grained model for biomolecular phase separation with near-quantitative accuracy. *Nat. Comput. Sci.* **2021**, *1*, 732–743.

(77) Nguyen, H. T.; Hori, N.; Thirumalai, D. Condensates in RNA repeat sequences are heterogeneously organized and exhibit reptation dynamics. *Nat. Chem.* **2022**, *14*, 775–785.

(78) Maity, H.; Zhang, H.; Thirumalai, D.; Nguyen, H. T. RNA Structural Complexity Dictates Its Ion Atmosphere. *J. Phys. Chem. Lett.* **2025**, 8393–8402.

(79) Nguyen, H. T.; Hori, N.; Thirumalai, D. Theory and simulations for RNA folding in mixtures of monovalent and divalent cations. *Proc. Natl. Acad. Sci. U.S.A.* **2019**, *116*, 21022–21030.

(80) Chandler, D.; Andersen, H. C. Optimized Cluster Expansions for Classical Fluids. II. Theory of Molecular Liquids. *J. Chem. Phys.* **1972**, *57*, 1930–1937.

(81) Hirata, F.; Rossky, P. J. An extended rism equation for molecular polar fluids. *Chem. Phys. Lett.* **1981**, *83*, 329–334.

(82) Luchko, T.; Gusarov, S.; Roe, D. R.; Simmerling, C.; Case, D. A.; Tuszynski, J.; Kovalenko, A. Three-Dimensional Molecular Theory of Solvation Coupled with Molecular Dynamics in Amber. *J. Chem. Theory Comput.* **2010**, *6*, 607–624.

(83) Luchko, T.; Joung, I. S.; Case, D. A. In *Innovations in Biomolecular Modeling and Simulations*; Schlick, T., Ed.; Royal Society of Chemistry, 2012; pp 51–86.

(84) Denesyuk, N. A.; Thirumalai, D. Coarse-Grained Model for Predicting RNA Folding Thermodynamics. *J. Phys. Chem. B* **2013**, *117*, 4901–4911.

(85) Weeks, J. D.; Chandler, D.; Andersen, H. C. Role of Repulsive Forces in Determining the Equilibrium Structure of Simple Liquids. *J. Chem. Phys.* **1971**, *54*, 5237–5247.

(86) DNA/RNA RasMol Tutorial. `https://www.biochem.umd.edu/kahn/teach_res/dna_tutorial/`.

(87) Xia, T.; SantaLucia, J. J.; Burkard, M. E.; Kierzek, R.; Schroeder, S. J.; Jiao, X.; Cox, C.; Turner, D. H. Thermodynamic Parameters for an Expanded Nearest-Neighbor Model for Formation of RNA Duplexes with Watson-Crick Base Pairs. *Biochemistry* **1998**, *37*, 14719–14735.

(88) Kast, S. M.; Kloss, T. Closed-form expressions of the chemical potential for integral equation closures with certain bridge functions. *J. Chem. Phys.* **2008**, *129*, 236101.

(89) Kovalenko, A.; Hirata, F. Self-consistent description of a metal–water interface by the Kohn–Sham density functional theory and the three-dimensional reference interaction site model. *J. Chem. Phys.* **1999**, *110*, 10095–10112.

(90) Perkyns, J.; Pettitt, B. M. A site–site theory for finite concentration saline solutions. *J. Chem. Phys.* **1992**, *97*, 7656–7666.

(91) Joung, I. S.; Luchko, T.; Case, D. A. Simple electrolyte solutions: Comparison of DRISM and molecular dynamics results for alkali halide solutions. *J. Chem. Phys.* **2013**, *138*, 044103.

(92) Malmberg, C. G.; Maryott, A. A. Dielectric constant of water from 0 to 100 °C. *J. Res. Natl. Bur. Stand.* **1956**, *56*, 1–8.

(93) Oosawa, F. *Polyelectrolytes*; M. Dekker, 1971.

(94) Manning, G. S. The molecular theory of polyelectrolyte solutions with applications to the electrostatic properties of polynucleotides. *Q. Rev. Biophys.* **1978**, *11*, 179–246.

(95) Record, M. T. J.; Anderson, C. F.; Lohman, T. M. Thermodynamic analysis of ion effects on the binding and conformational equilibria of proteins and nucleic acids: the roles of ion association or release, screening, and ion effects on water activity. *Q. Rev. Biophys.* **1978**, *11*, 103–178.

(96) Eastman, P. et al. OpenMM 8: Molecular Dynamics Simulation with Machine Learning Potentials. *J. Phys. Chem. B* **2024**, *128*, 109–116.

(97) Lipfert, J.; Doniach, S.; Das, R.; Herschlag, D. Understanding Nucleic Acid–Ion Interactions. *Annu. Rev. Biochem.* **2014**, *83*, 813–841.

(98) Kirkwood, J. G.; Buff, F. P. The Statistical Mechanical Theory of Solutions. I. *J. Chem. Phys.* **1951**, *19*, 774–777.

(99) Perry, Z. R.; Pyle, A. M.; Zhang, C. Arena: Rapid and Accurate Reconstruction of Full Atomic RNA Structures From Coarse-grained Models. *J. Mol. Biol.* **2023**, *435*, 168210.

(100) Pérez, A.; Marchán, I.; Svozil, D.; Sponer, J.; Cheatham, T. E.; Laughton, C. A.; Orozco, M. Refinement of the AMBER Force Field for Nucleic Acids: Improving the Description of $\alpha\gamma$ Conformers. *Biophys. J.* **2007**, *92*, 3817–3829.

(101) Svergun, D.; Barberato, C.; Koch, M. H. J. CRYSOL– a Program to Evaluate X-ray Solution Scattering of Biological Macromolecules from Atomic Coordinates. *J. Appl. Crystallogr.* **1995**, *28*, 768–773.

(102) Lavery, R.; Maddocks, J. H.; Pasi, M.; Zakrzewska, K. Analyzing ion distributions around DNA. *Nucleic Acids Res.* **2014**, *42*, 8138.

(103) Mitternacht, S. FreeSASA: An open source C library for solvent accessible surface area calculations. 2016; `https://f1000research.com/articles/5-189`.

(104) Lee, B.; Richards, F. M. The interpretation of protein structures: Estimation of static accessibility. *J. Mol. Biol.* **1971**, *55*, 379–IN4.

(105) Newby Lambert, M.; Vöcker, E.; Blumberg, S.; Redemann, S.; Gajraj, A.; Meiners, J.-C.; Walter, N. G. Mg^{2+}-Induced Compaction of Single RNA Molecules Monitored by Tethered Particle Microscopy. *Biophys. J.* **2006**, *90*, 3672–3685.

(106) Cantor, C. R.; Schimmel, P. R. *Biophysical Chemistry*; W. H. Freeman: San Francisco, 1980.

(107) Bloomfield, V. A.; Crothers, D. M.; Tinoco, I. *Nucleic Acids: Structures, Properties, and Functions*; University Science Books: Sausalito, 2000.

(108) Seol, Y.; Skinner, G. M.; Visscher, K.; Buhot, A.; Halperin, A. Stretching of Homopolymeric RNA Reveals Single-Stranded Helices and Base-Stacking. *Phys. Rev. Lett.* **2007**, *98*, 158103.

(109) Saenger, W. *Principles of Nucleic Acid Structure*; Springer-Verlag: New York, 1984.

(110) Spitale, R. C.; Incarnato, D. Probing the dynamic RNA structurome and its functions. *Nat. Rev. Genet.* **2023**, *24*, 178–196.

(111) Strobel, E. J.; Yu, A. M.; Lucks, J. B. High-throughput determination of RNA structures. *Nat. Rev. Genet.* **2018**, *19*, 615–634.

(112) Jacobson, D. R.; Saleh, O. A. Counting the ions surrounding nucleic acids. *Nucleic Acids Res.* **2017**, *45*, 1596–1605.

(113) Mondal, B.; Chakraborty, D.; Hori, N.; Nguyen, H. T.; Thirumalai, D. Competition between Stacking and Divalent Cation-Mediated Electrostatic Interactions Determines the Conformations of Short DNA Sequences. *J. Chem. Theory Comput.* **2024**, *20*, 2934–2946.

(114) Nguyen, H. T.; Thirumalai, D. Charge Density of Cation Determines Inner versus Outer Shell Coordination to Phosphate in RNA. *J. Phys. Chem. B* **2020**, *124*, 4114–4122.

(115) McDermott, M. L.; Vanselous, H.; Corcelli, S. A.; Petersen, P. B. DNA's Chiral Spine of Hydration. *ACS Cent. Sci.* **2017**, *3*, 708–714.

(116) Young, M. A.; Ravishanker, G.; Beveridge, D. L. A 5-nanosecond molecular dynamics trajectory for B-DNA: analysis of structure, motions, and solvation. *Biophys. J.* **1997**, *73*, 2313–2336.

(117) Liepinsh, E.; Otting, G.; Wüthrich, K. NMR observation of individual molecules of hydration water bound to DNA duplexes: direct evidence for a spine of hydration water present in aqueous solution. *Nucleic Acids Res.* **1992**, *20*, 6549–6553.

(118) Kopka, M. L.; Fratini, A. V.; Drew, H. R.; Dickerson, R. E. Ordered water structure around a B-DNA dodecamer. A quantitative study. *J. Mol. Biol.* **1983**, *163*, 129–146.

(119) Hori, N.; Denesyuk, N. A.; Thirumalai, D. Ion Condensation onto Ribozyme Is Site Specific and Fold Dependent. *Biophys. J.* **2019**, *116*, 2400–2410.

(120) Wang, T.; Coshic, K.; Badiee, M.; McDonald, M. R.; Aksimentiev, A.; Pollack, L.; Leung, A. K. L. Cation-induced intramolecular coil-to-globule transition in poly(ADP-ribose). *Nat. Commun.* **2024**, *15*, 7901.

(121) Eisenberg, H.; Felsenfeld, G. Studies of the temperature-dependent conformation and phase separation of polyriboadenylic acid solutions at neutral pH. *J. Mol. Biol.* **1967**, *30*, 17–37.

(122) Belaich, J. P.; Sari, J. C. Microcalorimetric studies on the formation of magnesium complexes of adenine nucleotides. *Proc. Natl. Acad. Sci. U.S.A.* **1969**, *64*, 763–770.

(123) Khan, M. M. T.; Martell, A. E. Thermodynamic quantities associated with the interaction of adenosinediphosphoric and adenosinemonophosphoric acids with metal ions. *J. Am. Chem. Soc.* **1967**, *89*, 5585–5590.

(124) Chen, S.; Wang, Z.-G. Driving force and pathway in polyelectrolyte complex coacervation. *Proc. Natl. Acad. Sci. U.S.A.* **2022**, *119*, e2209975119.

(125) Kilburn, D.; Behrouzi, R.; Lee, H.-T.; Sarkar, K.; Briber, R. M.; Woodson, S. A. Entropic stabilization of folded RNA in crowded solutions measured by SAXS. *Nucleic Acids Res.* **2016**, *44*, 9452–9461.

(126) Chang, L.-W.; Lytle, T. K.; Radhakrishna, M.; Madinya, J. J.; Vélez, J.; Sing, C. E.; Perry, S. L. Sequence and entropy-based control of complex coacervates. *Nat. Commun.* **2017**, *8*, 1273.

(127) Chowdhury, A.; Borgia, A.; Ghosh, S.; Sottini, A.; Mitra, S.; Eapen, R. S.; Borgia, M. B.; Yang, T.; Galvanetto, N.; Ivanović, M. T.; Łukijańczuk, P.; Zhu, R.; Nettels, D.; Kundagrami, A.; Schuler, B. Driving forces of the complex formation between highly charged disordered proteins. *Proc. Natl. Acad. Sci. U.S.A.* **2023**, *120*, e2304036120.

(128) Lin, Y.-H.; Chan, H. S. Phase Separation and Single-Chain Compactness of Charged Disordered Proteins Are Strongly Correlated. *Biophys. J.* **2017**, *112*, 2043–2046.

(129) Dignon, G. L.; Zheng, W.; Best, R. B.; Kim, Y. C.; Mittal, J. Relation between single-molecule properties and phase behavior of intrinsically disordered proteins. *Proc. Natl. Acad. Sci. U.S.A.* **2018**, *115*, 9929–9934.

(130) Zeng, X.; Holehouse, A. S.; Chilkoti, A.; Mittag, T.; Pappu, R. V. Connecting Coil-to-Globule Transitions to Full Phase Diagrams for Intrinsically Disordered Proteins. *Biophys. J.* **2020**, *119*, 402–418.

(131) Fang, X.-W.; Golden, B. L.; Littrell, K.; Shelton, V.; Thiyagarajan, P.; Pan, T.; Sosnick, T. R. The thermodynamic origin of the stability of a thermophilic ribozyme. *Proc. Natl. Acad. Sci. U.S.A.* **2001**, *98*, 4355–4360.

(132) Hu, E.-Z.; Lan, X.-R.; Liu, Z.-L.; Gao, J.; Niu, D.-K. A positive correlation between GC content and growth temperature in prokaryotes. *BMC Genomics* **2022**, *23*, 110.

(133) Nissley, A. J.; Penev, P. I.; Watson, Z. L.; Banfield, J. F.; Cate, J. H. D. Rare ribosomal RNA sequences from archaea stabilize the bacterial ribosome. *Nucleic Acids Res.* **2023**, *51*, 1880–1894.

(134) Becskei, A.; Rahaman, S. The life and death of RNA across temperatures. *Comput. Struct. Biotechnol. J.* **2022**, *20*, 4325–4336.

(135) Rissone, P.; Severino, A.; Pastor, I.; Ritort, F. Universal cold RNA phase transitions. *Proc. Natl. Acad. Sci. U.S.A.* **2024**, *121*, e2408313121.

(136) Ou, Z.; Muthukumar, M. Entropy and enthalpy of polyelectrolyte complexation: Langevin dynamics simulations. *J. Chem. Phys.* **2006**, *124*, 154902.

Coarse-grained Model of ssRNA with Explicit Mg^{2+}

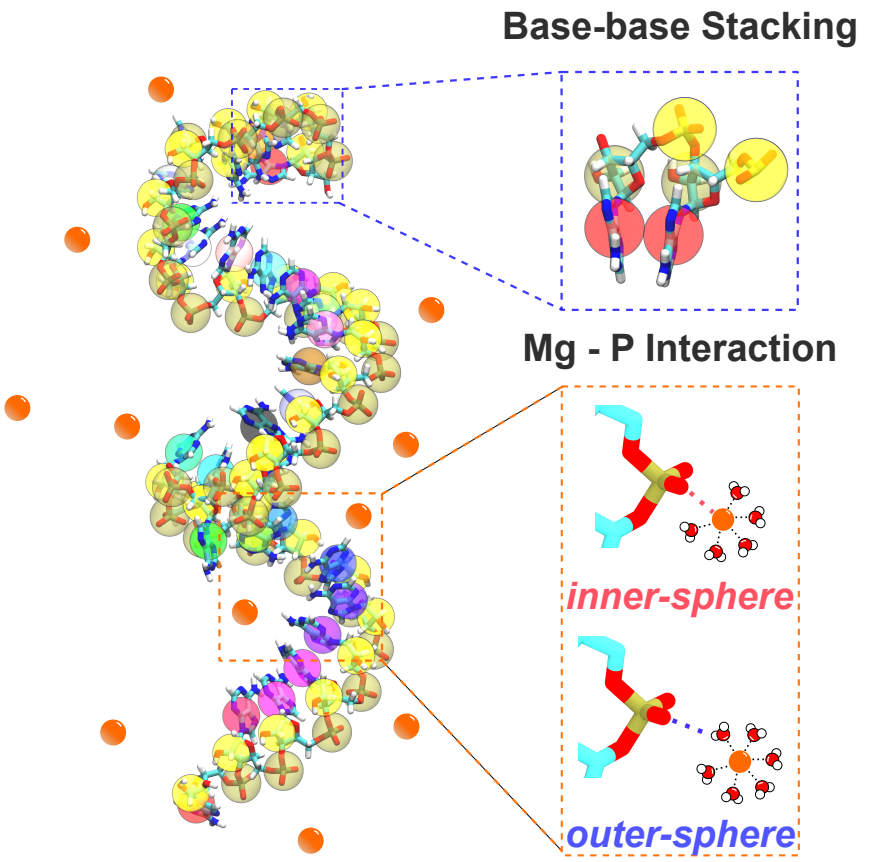

Temperature-dependent Mg^{2+} Binding

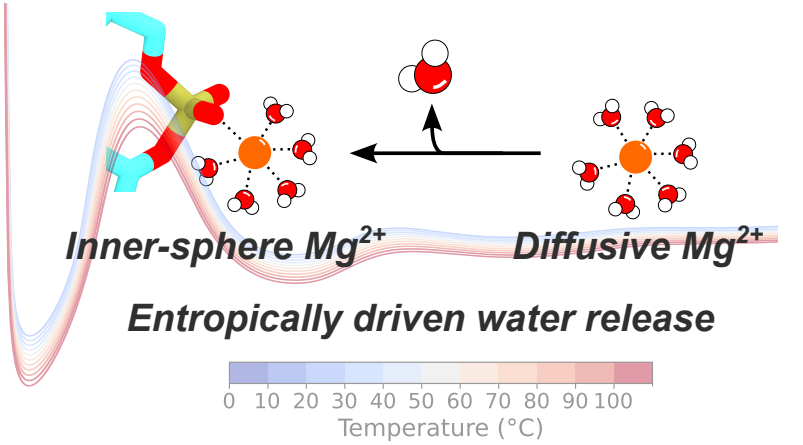
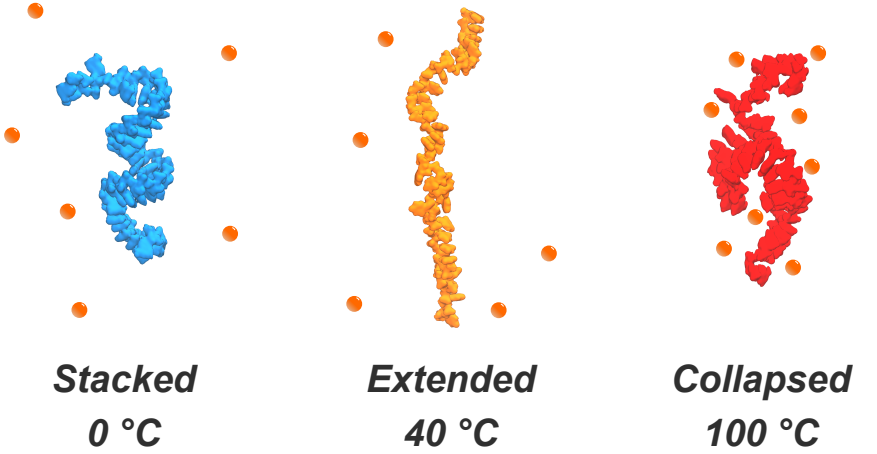
Sequence-dependent Thermal Collapse